

manuscript submitted to *Geophysical Research Letters*

# 1 Lower hybrid drift waves during guide field 2 reconnection

3 Jongsoo Yoo<sup>1</sup>, Jeong-Young Ji<sup>2</sup>, M. V. Ambat<sup>3</sup>, Shan Wang<sup>4</sup>, Hantao Ji<sup>5</sup>,  
4 Jensen Lo<sup>5</sup>, Bowen Li<sup>6</sup>, Yang Ren<sup>1</sup>, J. Jara-Almonte<sup>1</sup>, Li-Jen Chen<sup>4</sup>, William  
5 Fox<sup>1</sup>, Masaaki Yamada<sup>1</sup>, Andrew Alt<sup>1</sup>, Aaron Goodman<sup>1</sup>

6 <sup>1</sup>Princeton Plasma Physics Laboratory, Princeton, New Jersey 08543, USA.

7 <sup>2</sup>Department of Physics, Utah State University, Logan, Utah 84322, USA.

8 <sup>3</sup>Department of Mechanical Engineering, University of Rochester, Rochester, NY 14627, USA.

9 <sup>4</sup>NASA Goddard Space Flight Center, Greenbelt, Maryland 20771, USA.

10 <sup>5</sup>Department of Astrophysical Sciences, Princeton University, Princeton, NJ 08544, USA.

11 <sup>6</sup>Harbin Institute of Technology, Harbin, China.

## 12 Key Points:

- 13 The short-wavelength lower hybrid wave is observed inside a current sheet during guide field reconnection.
- 14 Theoretical model for the dispersion relation of the lower hybrid wave based on local geometry is developed.
- 15 Free energy source for the lower hybrid wave is the perpendicular current and high beta stabilizes the wave.

19 **Abstract**

20 Generation and propagation of lower hybrid drift wave (LHDW) within and near the elec-  
 21 tron diffusion region (EDR) during guide field reconnection at the magnetopause is stud-  
 22 ied with data from the Magnetospheric Multiscale mission and a theoretical model. In-  
 23 side the EDR where the electron beta is high ( $\beta_e \sim 5$ ), the long-wavelength electromag-  
 24 netic LHDW propagating obliquely to the local magnetic field is observed. In contrast,  
 25 the short-wavelength electrostatic LHDW propagating nearly perpendicular to the lo-  
 26 cal magnetic field is observed slightly away from the EDR, where  $\beta_e$  is small ( $\sim 0.6$ ).  
 27 These observed LHDW features are explained by a local theoretical model only after in-  
 28 cluding effects from the electron temperature anisotropy, finite electron heat flux and par-  
 29 allel current. The short-wavelength LHDW is capable of generating significant drag force  
 30 between electrons and ions.

31 **1 Introduction**

32 Magnetic reconnection (Yamada, Kulsrud, & Ji, 2010) rapidly releases magnetic  
 33 energy through topological rearrangement of magnetic field lines. In the diffusion region  
 34 where reconnection occurs, there are various free energy sources for waves and instabil-  
 35 ities. In particular, the lower hybrid drift wave (LHDW) has been observed frequently  
 36 near the diffusion region in both laboratory (e.g. Carter, Ji, Trintchouk, Yamada, & Kul-  
 37 srud, 2001; H. Ji et al., 2004; Yoo, Yamada, Ji, Jara-Almonte, Myers, & Chen, 2014) and  
 38 space (e.g. Chen et al., 2019; Graham et al., 2017; Norgren, Vaivads, Khotyaintsev, &  
 39 André, 2012). The fast-growing, short-wavelength ( $k\rho_e \sim 1$ ;  $k$  is the magnitude of the  
 40 wave vector  $\mathbf{k}$ ;  $\rho_e$  is the electron gyroradius), electrostatic LHDW propagating nearly  
 41 perpendicular to the local magnetic field ( $\mathbf{B}_0$ ) does not exist near the electron diffusion  
 42 region (EDR) during antiparallel reconnection (Carter et al., 2001; Roytershteyn, Daughton,  
 43 Karimabadi, & Mozer, 2012; Roytershteyn et al., 2013) due to the stabilization by the  
 44 high plasma beta ( $\beta$ ) (Davidson, Gladd, Wu, & Huba, 1977). The long-wavelength ( $k\sqrt{\rho_e\rho_i} \sim$   
 45 1;  $\rho_i$  is the ion gyroradius) electromagnetic LHDW propagating obliquely to  $\mathbf{B}_0$  is ob-  
 46 served in the EDR (H. Ji et al., 2004; Roytershteyn et al., 2012) but it does not play an  
 47 important role in fast reconnection under typical magnetosphere conditions (Roytershteyn  
 48 et al., 2012).

49 In general, reconnection occurs with guide field, which is a relatively uniform out-  
 50 of-plane magnetic field component. The presence of the guide field impacts the struc-

ture of the diffusion region and electron and ion dynamics (Fox et al., 2017; Pritchett & Coroniti, 2004; Ricci, Blackbill, Daughton, & Lapenta, 2004; Tharp et al., 2012). Moreover, the guide field can reduce  $\beta$  in the EDR, such that the fast-growing, short-wavelength LHDW can exist in the EDR, potentially impacting on reconnection and electron dynamics.

Here we demonstrate that the short-wavelength LHDW is generated near the EDR by analyzing data from the Magnetospheric Multiscale (MMS) mission. In this event, there is a moderate guide field ( $B_g \sim 0.5B_{rec}$ ;  $B_g$  is the guide field magnitude;  $B_{rec}$  is the reconnecting field magnitude). Inside the EDR where  $\beta_e$  is high ( $\sim 5$ ), the long-wavelength LHDW is present, while the short-wavelength LHDW is excited slightly away from the EDR where  $\beta_e$  is about 0.6.

Observed LHDW activity are explained by a local theoretical model, improved from a previous model (H. Ji, Kulsrud, Fox, & Yamada, 2005) by including important effects from the electron temperature anisotropy, finite electron heat flux for the parallel temperature, and parallel electron flow. This model address LHDW with an arbitrary angle between  $\mathbf{k}$  and  $\mathbf{B}_0$  unlike the classical formulation (Davidson et al., 1977). Results from the model agree with measured characteristics of the short-wavelength LHDW;  $\mathbf{k}$  is nearly perpendicular to  $\mathbf{B}_0$  at  $k\rho_e \sim 0.7$ . The short-wavelength LHDW produces significant drag force between electrons and ions. This study proves that the short-wavelength LHDW can be excited within the EDR under a sufficiently large guide field, potentially affecting electron and reconnection dynamics.

## 2 Overview of the MMS Event with LHDW

An overview of a magnetopause event observed by MMS2 on December 14, 2015 (Chen et al., 2017; Ergun et al., 2017) is shown in Fig. 1. Here we use burst-mode data from the Fluxgate Magnetometer (FGM) (Russell et al., 2016), Search Coil Magnetometer (SCM) (Le Contel et al., 2016), the electric field spin plane (Lindqvist et al., 2016), axial double probes (Ergun et al., 2016), and Fast Plasma Investigation (FPI) (Pollock et al., 2016). Two magenta vertical lines denote two regions, where the local dispersion relation for LHDW is calculated. The region A represents the EDR (Chen et al., 2017; Ergun et al., 2017), while B is slightly outside the EDR.

The magnetic field profile measured by FGM is shown in Fig. 1(a). The transformation matrix from the geocentric solar ecliptic coordinate to the local  $LMN$  coordi-

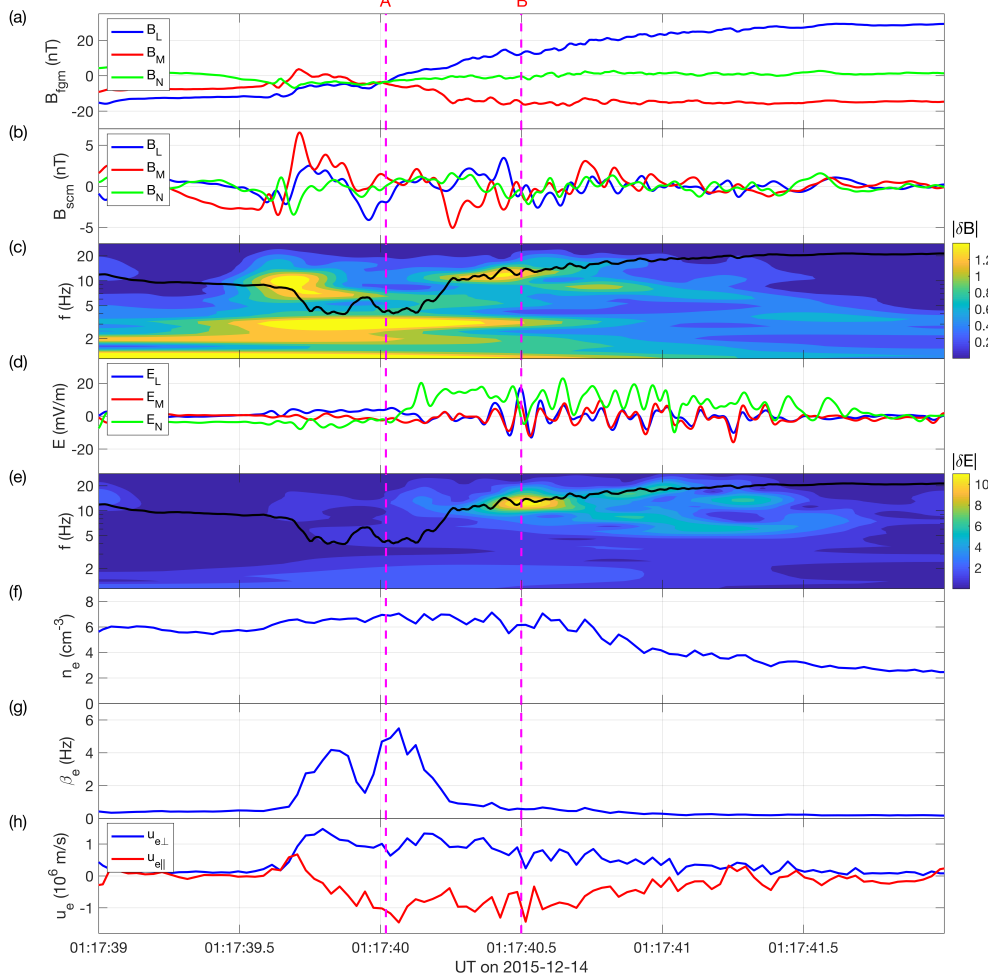


**Figure 1.** Overview of a magnetopause event with LHDW activity observed by MMS2. Two magenta dashed lines denoted by A and B indicate the time where LHDW stability analysis is performed. The region A represents the EDR, while the region B is slightly outside the EDR. (a) Magnetic field profile measured by FGM. Across the current sheet, there is an average negative  $B_M$  component. (b) Magnetic field profile measured by SCM, filtered by a low-pass filter with a cutoff frequency of 40 Hz. (c) Magnetic field spectrogram by the Morlet wavelet. The black line indicates  $f_{LH}$ . Fluctuations in the magnetic field persists throughout the current sheet crossing (01:17:39.7 – 01:17:41.5). In the region A, the fluctuations is below  $f_{LH}$ . (d) Electric field profile filtered by the same filter. There are strong fluctuations around the region B. (e) Electric field spectrogram by the wavelet analysis, which demonstrates fluctuations near  $f_{LH}$  around the region B. (f) Electron density profile. Density fluctuations exist near B. (g) Profile of  $\beta_e$ . In the region A,  $\beta_e$  is high, while it becomes small around the region B. (h) Profile of the electron flow. Both parallel (red) and perpendicular (blue) components exist throughout the current sheet crossing.

83 nate system is  $(L, M, N) = ([0.095, -0.481, 0.865], [-0.445, -0.811, -0.392], [0.889, -0.346, -0.290])$ ,  
 84 which is obtained by a hybrid method (Yoo & Yamada, 2012) using both the minimum  
 85 variance analysis and timing analysis, particularly with the assumption of the constant  
 86 thickness (Haaland et al., 2004). The current sheet thickness for this event is about 130  
 87 km, which is larger than the ion skin depth  $d_i$  in the region B ( $\sim 90$  km). The region  
 88 A is close to the reversal of the reconnecting field component  $B_L$ , while the region B is  
 89 shifted to the low-density side. Note that there is a density asymmetry across the cur-  
 90 rent sheet with a ratio of about 3, as shown in Fig. 1(f). Profiles of  $B_L$  and the electron  
 91 flow  $\mathbf{u}_e$  in Fig. 1(h) suggest that MMS2 passes through the current sheet from 01:17:39.7  
 92 to 01:17:41.5.

93 The out-of-plane magnetic field component  $B_M$  has a negative value on average,  
 94 indicating there is a guide field for this event. The large perturbation of  $B_M$  from 01:17:39.7  
 95 to 01:17:40.3 in Fig. 1(a) is due to the bipolar Hall field structure in asymmetric recon-  
 96 nection (Mozer, Angelopoulos, Bonnell, Glassmeier, & McFadden, 2008; Pritchett, 2008;  
 97 Yoo, Yamada, Ji, Jara-Almonte, & Myers, 2014). Excluding this variation, the guide field  
 98 strength is about 14 nT. Considering the asymmetry (Cassak & Shay, 2007),  $B_{\text{rec}}$  is about  
 99 28 nT. Thus,  $B_g \sim 0.5B_{\text{rec}}$ .

100 Near the region A, as shown in Fig. 1 (b) and (c), fluctuations in the magnetic field  
 101  $\mathbf{B}$  below the local lower hybrid frequency ( $f_{\text{LH}}$ , denoted by the black line in (c)) exist.  
 102 Fluctuations in the electric field  $\mathbf{E}$  and electron density  $n_e$  are not strong, as shown in  
 103 Fig. 1 (d) and (f). Around the region B, as shown in Fig. 1(b)–(f), there are fluctuations  
 104 in  $\mathbf{B}$ ,  $\mathbf{E}$ , and  $n_e$  near  $f_{\text{LH}}$ . As shown in spectrograms of  $\mathbf{B}$  and  $\mathbf{E}$  in Fig. 1(c) and (e),  
 105 most power of the fluctuations exist close to  $f_{\text{LH}}$ .

106 Figures 1(g) and (h) shows the profile of  $\beta_e$  and the electron flow vector  $\mathbf{u}_e$ , respec-  
 107 tively. Values of  $\beta_e$  are different in two regions; about 4.2 in A and 0.6 in B. Values of  
 108  $\mathbf{u}_e$ , in contrast, are similar. Note that both the perpendicular and parallel components  
 109 of  $\mathbf{u}_e$  are significant. The observed features of fluctuations in the region B can be explained  
 110 by the short-wavelength LHDW. First, the perpendicular electron flow  $\mathbf{u}_{e\perp}$  is large. Sec-  
 111 ond, the mode exists when  $\beta_e$  is small. Finally, the frequency of the wave is around  $f_{\text{LH}}$ .

### 112 3 Calculation of the LHDW dispersion relation

113 The geometry of our local model is similar to that of H. Ji et al. (2005);  $z$  is along  
 114  $\mathbf{B}_0$ , and  $y$  is along the density gradient direction in the ion rest frame. The wave vec-

115 tor is assumed on the  $x$ - $z$  plane with an assumption of negligible  $k_y$ . Unlike H. Ji et al.  
 116 (2005), the equilibrium electron flow velocity ( $\mathbf{u}_{e0}$ ) has a parallel component ( $u_{e0z}$ ). Equi-  
 117 librium temperature is assumed to be uniform and ion temperature anisotropy is ignored.

The detailed derivation of the dispersion relation is provided in the supporting information. Here only important improvements over the model in H. Ji et al. (2005) are discussed. First, for the quasi-electrostatic nature of the short-wavelength LHDW, the perturbed electron density  $n_{e1}$  is independently obtained from the electron continuity equation:

$$(\omega - \mathbf{k} \cdot \mathbf{u}_{e0})n_{e1} = (\mathbf{k} \cdot \mathbf{u}_{e1} - i\epsilon u_{e1y})n_{e0}, \quad (1)$$

118 where the subscript 1 indicates perturbed quantities,  $\mathbf{u}_{e1}$  is the perturbed electron flow  
 119 velocity,  $n_{e0}$  is the equilibrium density, and  $\epsilon = (dn_{e0}/dy)/n_{e0}$  is the inverse of the den-  
 120 sity gradient scale. The electron temperature anisotropy is also taken into account;  $T_{e0}^\perp \neq$   
 121  $T_{e0}^\parallel$ , where  $T_{e0}^\perp$  and  $T_{e0}^\parallel$  are the perpendicular and parallel electron equilibrium temper-  
 122 ature, respectively.

123 The perturbed perpendicular electron pressure is assumed to be  $p_{e1}^\perp \approx n_{e1}T_{e0}^\perp$ , which  
 124 means that the perpendicular temperature perturbation is ignored (isothermal limit).  
 125 This simplification is justifiable because LHDW stability does not much depend on the  
 126 specific form of  $p_{e1}^\perp$ ; other terms such as  $\mathbf{E}_1$ ,  $\mathbf{u}_{e1} \times \mathbf{B}_0$ , and  $\mathbf{u}_{e0} \times \mathbf{B}_1$  are more impor-  
 127 tant for the electron momentum balance along the perpendicular direction. Here,  $\mathbf{E}_1$  and  
 128  $\mathbf{B}_1$  are the perturbed electric and magnetic field, respectively. This isothermal limit im-  
 129 plies infinite heat flux for the perpendicular temperature. We find that the dispersion  
 130 relation does not change much even in the limit of the zero heat flux.

For the parallel direction, however, more rigorous treatment of the electron heat flux is required, as the perturbed electron parallel pressure  $p_{e1}^\parallel$  becomes important for the electron force balance due to the absence of  $\mathbf{u}_{e1} \times \mathbf{B}_0$  term. To obtain  $p_{e1}^\parallel$ , we start from the following equation from the Vlasov equation:

$$\frac{\partial p_e^\parallel}{\partial t} + \nabla \cdot (\mathbf{u}_e p_e^\parallel) + \nabla \cdot \mathbf{q}_e^\parallel + 2 \frac{\partial u_{ez}}{\partial z} p_e^\parallel = 0, \quad (2)$$

131 where  $p_e^\parallel = m_e \int (v_z - u_{ez})^2 f_e d\mathbf{v}$ ,  $\mathbf{q}_e^\parallel = m_e \int (\mathbf{v} - \mathbf{u}_e) (v_z - u_{ez})^2 f_e d\mathbf{v}$ , and  $n_e \mathbf{u}_e =$   
 132  $\int \mathbf{v} f_e d\mathbf{v}$ . Note that  $\mathbf{q}_e^\parallel$  is the electron heat flux affecting the parallel electron temper-  
 133 ature rather than the parallel heat flux.

A closure for  $\mathbf{q}_e^{\parallel}$  is required for  $p_{e1}^{\parallel}$ . The 3+1 fluid model (J.-Y. Ji & Joseph, 2018) gives

$$\mathbf{q}_e^{\parallel} = \frac{\hat{z}}{m_e \omega_{ce}} \times \left( p_e^{\parallel} \nabla T_e + T_e \nabla p_e^{\parallel} - \frac{T_e}{2} \nabla \pi_e^{\parallel} - T_e^{\parallel} \nabla p_e^{\perp} \right) + q_{ez}^{\parallel} \hat{z}, \quad (3)$$

where  $\pi_e^{\parallel} = 2(p_e^{\parallel} - p_e^{\perp})/3$ , and  $T_e = (2T_e^{\perp} + T_e^{\parallel})/3$ . The derivation of this equation is also given in the supporting information. The closure for  $q_{e1z}^{\parallel}$  in the collisionless limit is J.-Y. Ji and Joseph (2018)

$$q_{e1z}^{\parallel} = \frac{-i}{\sqrt{\pi}} \frac{k_{\parallel}}{|k_{\parallel}|} 2n_0 v_{te} T_{e1}^{\parallel}, \quad (4)$$

where  $T_{e1}^{\parallel} = (p_{e1}^{\parallel} - T_{e0}^{\parallel} n_1)/n_0$  is the perturbed parallel temperature and  $v_{te} = \sqrt{2T_{e0}/m_e}$  is the electron thermal speed. By linearizing Eq. 3,  $q_{e1x}^{\parallel}$  becomes

$$q_{e1x}^{\parallel} = -\frac{2}{9} \frac{(T_{e0}^{\parallel} - 4T_{e0}^{\perp}) T_{e1}^{\parallel}}{T_{e0}^{\perp} + T_{i0}} n_0 u_{e0x} = r_e^{\parallel} T_{e1}^{\parallel} n_0 u_{e0x}, \quad (5)$$

where  $r_e^{\parallel} = 2(4T_{e0}^{\perp} - T_{e0}^{\parallel})/9(T_{e0}^{\perp} + T_{i0})$ . With Eqs. 2, 4, and 5,  $p_{e1}^{\parallel}$  is given by

$$p_{e1}^{\parallel} = n_{e1} T_{e0}^{\parallel} + \frac{2k_{\parallel} n_0 T_{e0}^{\parallel} u_{e1z}}{\omega - \mathbf{k} \cdot \mathbf{u}_{e0} - r_e^{\parallel} k_{\perp} u_{e0x} + i(2/\sqrt{\pi}) |k_{\parallel}| v_{te}}. \quad (6)$$

With these closures, the electron momentum equation is solved to obtain the perturbed electron current density,  $\mathbf{J}_{e1}$ . The ion current is given by the Eq. (8) in the Ref. (H. Ji et al., 2005). With  $\mathbf{J}_1 = \mathbf{J}_{e1} + \mathbf{J}_{i1}$ , the Maxwell equation without the displacement current  $\mathbf{k} \times (\mathbf{k} \times \mathbf{E}_1) = -i\omega\mu_0\mathbf{J}_1$  can be expressed as

$$\begin{pmatrix} D_{xx} & D_{xy} & D_{xz} \\ D_{yx} & D_{yy} & D_{yz} \\ D_{zx} & D_{zy} & D_{zz} \end{pmatrix} \begin{pmatrix} E_{1x} \\ E_{1y} \\ E_{1z} \end{pmatrix} = 0, \quad (7)$$

with a tensor  $\mathbf{D}$ . The dispersion relation for the wave can be obtained from  $\det \mathbf{D} = 0$ . The calculation for each component of  $\mathbf{D}$  is provided in the supporting information.

Dispersion relations are obtained with plasma parameters measured in the region A and B. For the region A, parameters averaged over 01:17:39.989–01:17:40.049 are  $B_0 = 6.5$  nT,  $n_0 = 6.1 \text{ cm}^{-3}$ ,  $T_{e0}^{\parallel} = 79.5 \text{ eV}$ ,  $T_{e0}^{\perp} = 70.9 \text{ eV}$ ,  $T_{i0} = 395 \text{ eV}$ ,  $u_{e0x} = 17.9 V_A$ , and  $u_{e0z} = -14.1 V_A$ , where  $V_A = 57.7 \text{ km/s}$  is the local Alfvén speed. With these values,  $\beta_e = 4.24$  and  $f_{LH} = 4.4 \text{ Hz}$ . For the region B, parameters averaged over 01:17:40.469–529 are  $B_0 = 19.8 \text{ nT}$ ,  $n_0 = 6.2 \text{ cm}^{-3}$ ,  $T_{e0}^{\parallel} = 122 \text{ eV}$ ,  $T_{e0}^{\perp} = 77.6 \text{ eV}$ ,  $T_{i0} = 402 \text{ eV}$ ,  $u_{e0x} = 2.65 V_A$ , and  $u_{e0z} = -5.07 V_A$  with  $V_A = 174 \text{ km/s}$ ,  $\beta_e = 0.58$ , and  $f_{LH} = 12.9 \text{ Hz}$ .

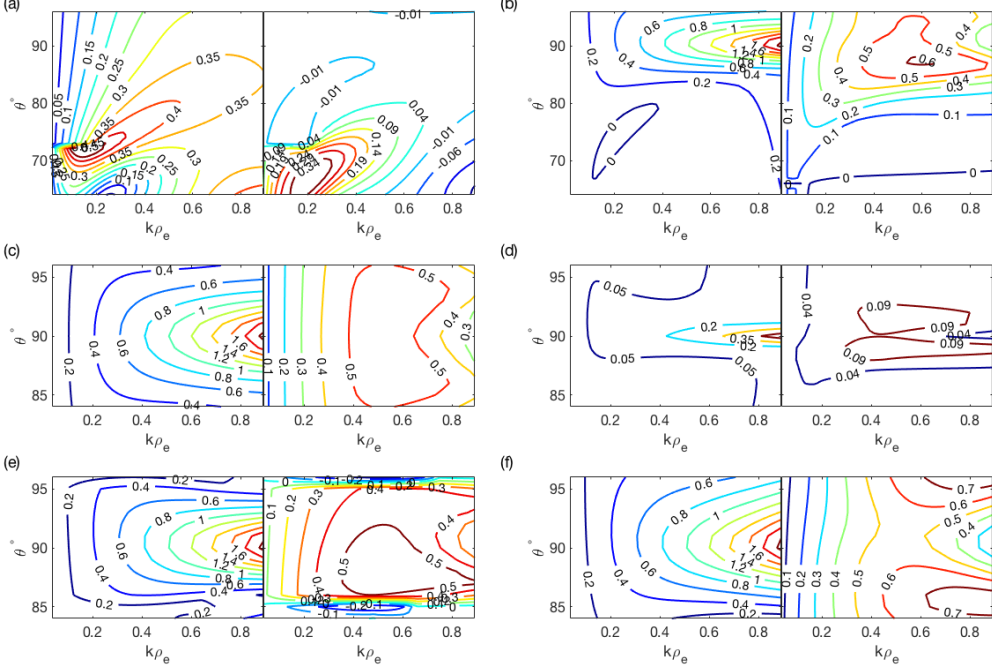


**Figure 2.** Dispersion relation of LHDW. For each subplot, the left (right) panel shows the contour plot for the real (imaginary) part of the angular frequency normalized by the local lower hybrid frequency  $\omega_{\text{LH}}$  as a function of  $k\rho_e$  and  $\theta$ . Here  $\rho_e$  is the electron gyroradius in the region B even for the axis of panels (a). (a) In the region A, the long-wavelength LHDW ( $\theta \sim 70^\circ$ ) is unstable, while the short-wavelength LHDW is marginally stable due to high  $\beta$ . (b) In the region B, the short-wavelength LHDW has fast growth rates  $\gamma \sim 0.6\omega_{\text{LH}}$  with  $\Re(\omega) \sim \omega_{\text{LH}}$ . (c) Without the parallel flow, the dispersion becomes symmetric with respect to  $\theta = 90^\circ$  but there is no significant change in  $\gamma$ . (d) When the perpendicular flow is reduced to  $0.7V_A$ ,  $\gamma$  becomes much smaller, which indicates  $u_{e0x}$  is the free energy source. The range of  $\theta$  is different for panels (c) and (d). (e) Without  $q_e^{\parallel}$ , oblique modes are stabilized. (f) Without  $T_{e1}^{\parallel}$  (infinite heat flux),  $\gamma$  becomes even larger especially for more oblique modes, which shifts  $\Re(\omega)$  with the maximum  $\gamma$  to about  $0.4\omega_{\text{LH}}$ .

144 The calculated dispersion relation is shown in Fig. 2(a); the left (right) panel shows  
 145 the real (imaginary) part of the angular frequency as a function of  $k$  and  $\theta$ , which is nor-  
 146 malized by the local (angular) lower hybrid frequency,  $\omega_{\text{LH}}$ . In the region A, the short-  
 147 wavelength LHDW around  $\theta = 90^\circ$  is marginally stable despite the strong electron flow.  
 148 The long-wavelength LHDW around  $\theta = 70^\circ$ , in contrast, is unstable around  $f < 0.5f_{\text{LH}}$ ,  
 149 which agrees with measurements in Fig. 1(c).

150 In the region B, the short-wavelength LHDW has large growth rates with the max-  
 151 imum growth rate  $\gamma_{\text{max}} \sim 0.6\omega_{\text{LH}}$ , as shown in Fig. 2(b). The frequency around  $\gamma_{\text{max}}$   
 152 is  $\sim 0.8f_{\text{LH}}$ . The model expects  $k_{\perp} \gg |k_{\parallel}|$ . All these features are consistent with those  
 153 of the short-wavelength LHDW (Davidson et al., 1977).

154 This model indicates that the free energy source is the perpendicular current. Even  
 155 with zero parallel electron velocity, the dispersion expects similar  $\gamma$ , as shown in Fig. 2(c).  
 156 When the perpendicular velocity is decreased from  $2.65V_{\text{A}}$  to  $0.7V_{\text{A}}$ , however,  $\gamma$  becomes  
 157 small, as shown in Fig. 2(d). If  $u_{e0x}$  is reduced below  $0.5V_{\text{A}}$ , the mode disappears.

To understand the effect of  $\mathbf{q}_e^{\parallel}$  on the dispersion, we have tested two limits – no  
 155 heat flux and infinite heat flux. Without the heat flux,  $p_{e1}^{\parallel}$  in Eqn. 6 becomes

$$p_{e1}^{\parallel} = n_{e1} T_{e0}^{\parallel} + \frac{2k_{\parallel} n_0 T_{e0}^{\parallel} u_{e1z}}{\omega - \mathbf{k} \cdot \mathbf{u}_{e0}}. \quad (8)$$

158 With the infinite heat flux ( $v_{th} \rightarrow \infty$ ),  $p_{e1}^{\parallel} = n_{e1} T_{e0}^{\parallel}$ , which means  $T_{e1}^{\parallel} = 0$ . Figure 2  
 159 (e) and (f) show the dispersion for these two limits. When  $\theta$  is close to  $90^\circ$ , results are  
 160 not affected. For oblique modes, however, the heat flux significantly affects the disper-  
 161 sion relation, especially the growth rate. Without  $\mathbf{q}_e^{\parallel}$ , oblique modes are quickly stabi-  
 162 lized; as shown in the bottom panel of Fig. 2(e),  $\gamma$  becomes negative for  $\theta \sim 85^\circ$  or  $\theta \sim$   
 163  $96^\circ$ . With the infinite heat flux (zero  $T_{e1}^{\parallel}$ ), on the other hand,  $\gamma$  for oblique modes be-  
 164 comes larger than values in Fig. 2(b), as shown in Fig. 2(f).

165 This dependence of  $\gamma$  on  $\mathbf{q}_e^{\parallel}$  can be understood by the parallel force balance. The  
 166 perturbed pressure term,  $ikp_{e1}^{\parallel}$  can be interpreted as a restoring force against the elec-  
 167 tric field perturbation. The heat flux reduces the temperature perturbation, which means  
 168 that the restoring force decreases as the heat flux increases. Thus, in the limit of the in-  
 169 finite (zero) heat flux,  $\gamma$  becomes larger (smaller) for oblique modes.

## 170 4 Comparison between theory and observation

171 The dispersion relation is crucial for identifying the wave and understanding its prop-  
 172 agation. If all MMS satellites observed the same wave packet,  $\mathbf{k}$  could be estimated di-

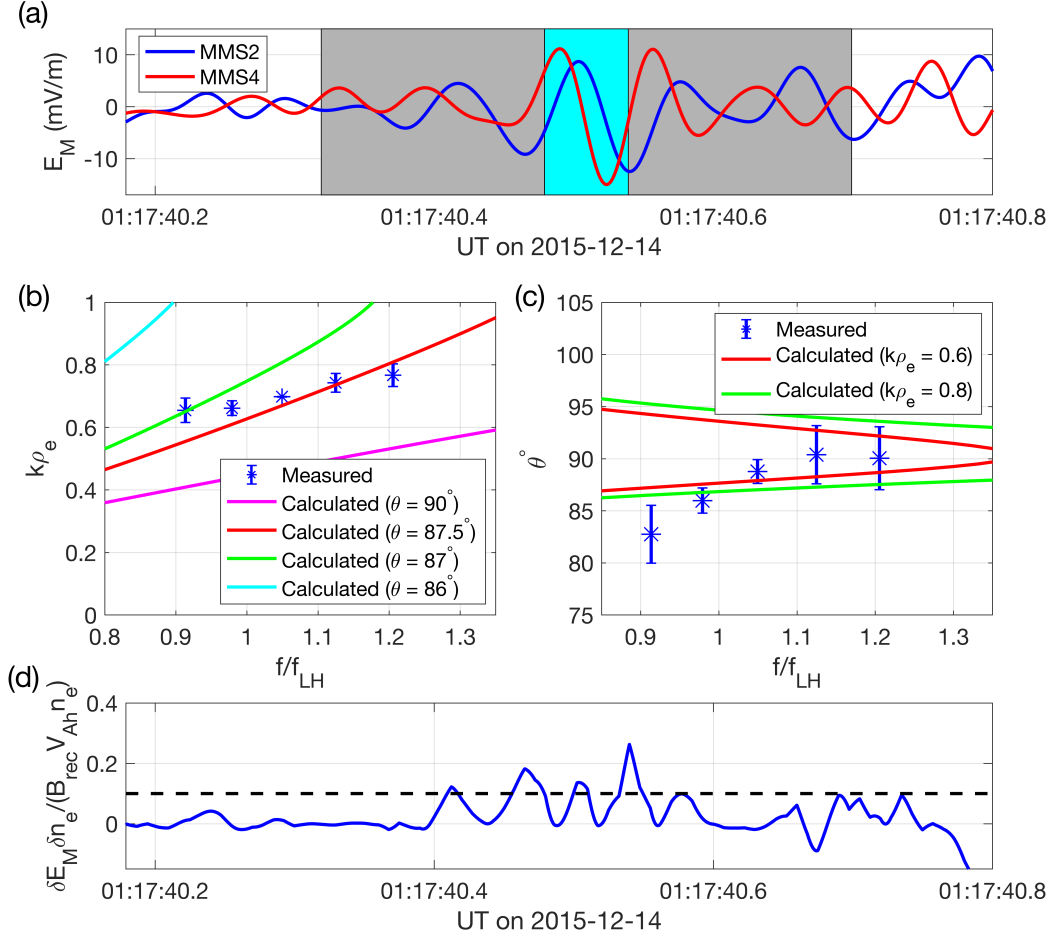


**Figure 3.** Wave vector measurement and comparison with the theory. (a) Profile of  $E_M$  near the region B, which is filtered by a low-pass filter with a cutoff frequency of 40 Hz. Signals from MMS2 and MMS4 correlate. The cyan box indicates the period where the analysis for the wave vector is performed. The gray box indicates the range of data used for the wavelet analysis. (b) Magnitude of the wave vector. Blue asterisks are measured values ( $k\rho_e \sim 0.7$ ). Theoretical values with various  $\theta$  are plotted with solid lines. (c) Angle between  $\mathbf{k}$  and  $\mathbf{B}_0$ . Blue asterisks are values estimated by the SVD analysis. Theoretical values with various  $k$  are plotted with solid lines. The wave propagates almost perpendicular to  $\mathbf{B}_0$ . Error bars in (b) and (c) are from the standard deviation of the values computed during the period indicated by the cyan box in (a). Frequency values in (b) and (c) are the central frequency of the Morlet wavelet. (d) Anomalous drag by LHDW.  $\delta E_M \delta n_e$  is normalized by  $B_{rec} V_{Ah} n_e$ . The black dashed line represents the nominal normalized reconnection rate for collisionless reconnection, 0.1 (Birn et al., 2001).

173 rectly from the phase difference (Yoo et al., 2018). However, for this event, signals from  
 174 only MMS2 and MMS4 have correlation, while they are near the region B. Thus, single  
 175 spacecraft methods such as the singular value decomposition (SVD) analysis (Santolík,  
 176 Parrot, & Lefèuvre, 2003) should be considered.

177 The SVD analysis has its own caveat; this method relies on the assumption that  
 178 there is only one dominant  $\mathbf{k}$  for a given frequency. This assumption is not valid for LHDW;  
 179 as shown in Fig. 2(b), there is a range of  $k$  and  $\theta$  that has a positive growth rate for a  
 180 given frequency. In this case, the estimated  $\mathbf{k}$  is a power-weighted average of multiple  
 181 wave vectors, which underestimates the magnitude of  $\mathbf{k}$  (Yoo et al., 2019). The direc-  
 182 tion of the estimated  $\mathbf{k}$ , on the other hand, still indicates the average propagation di-  
 183 rection.

The wave vector  $\mathbf{k}$  is estimated by combining two methods. With the unit vector  
 $\hat{\mathbf{k}}$  from the SVD analysis, the magnitude  $k$  is

$$k = \frac{\phi_2 - \phi_4}{\hat{\mathbf{k}} \cdot (\mathbf{r}_2 - \mathbf{r}_4)}, \quad (9)$$

184 where  $\phi_2$  and  $\phi_4$  are the phase of the correlated signal measured by MMS2 and MMS4,  
 185 while  $\mathbf{r}_2$  and  $\mathbf{r}_4$  are the location of MMS2 and MMS4, respectively. The phase informa-  
 186 tion comes from the Morlet wavelet transform of  $E_M$  (Torrence & Compo, 1998). As shown  
 187 in Fig. 3(a),  $E_M$  signals from two satellites are correlated in the region B (cyan box).

188 Figure 3(b) shows the measured  $k\rho_e$  (blue asterisks), compared with theoretical val-  
 189 ues (solid lines). For theoretical values, the Doppler shift due to the frame difference is  
 190 considered, which is  $\Delta f = \mathbf{u}_i \cdot \mathbf{k}/2\pi$ . Here  $\mathbf{u}_i$  is the ion flow velocity in the spacecraft  
 191 frame ( $u_{ix} = 33$  km/s,  $u_{iz} = -38$  km/s). At  $f = 0.98f_{\text{LH}}$ ,  $k\rho_e = 0.66$ , which agrees  
 192 with the theoretical value with  $\theta \sim 87^\circ$ . Note that the mode with the highest growth  
 193 rate exists around  $\theta \sim 87^\circ$  and  $k\rho_e \sim 0.6$ , as shown in Fig. 2(b).

194 Figure 3(c) shows the measured  $\theta$  (blue asterisks), compared with theoretical val-  
 195 ues of various  $k$  (solid lines). The measurement shows that LHDW propagates almost  
 196 perpendicular to  $\mathbf{B}_0$ , which agrees with the model. The measured  $\hat{\mathbf{k}}$  has a dominant com-  
 197 ponent along the  $x$  direction ( $\hat{\mathbf{k}} = (0.987, -0.155, -0.019)$  for  $f = 1.05f_{\text{LH}}$ ), which sup-  
 198 ports the ignorance of  $k_y$ .

199 The short-wavelength LHDW generates correlated fluctuations of the electron den-  
 200 sity and electric field, generating anomalous drag force between electrons and ions (Mozer,  
 201 Wilber, & Drake, 2011). Figure 3(d) shows  $\delta E_M \delta n_e$ , normalized by  $B_{\text{rec}} V_{\text{Ah}} \langle n_e \rangle$ , where  
 202  $V_{\text{Ah}} = 274$  km/s is the hybrid upstream Alfvén velocity for asymmetric reconnection

(Cassak & Shay, 2007). Here the angle bracket means the average of a quantity  $A$  from 01:17:40.2 to 01:17:40.8 and a fluctuating quantity is defined as  $\delta A = A - \langle A \rangle$ . Two fluctuating quantities  $\delta E_M$  and  $\delta n_e$  are correlated, producing a positive net value of  $\delta E_M \delta n_e$ , especially from 01:17:40.4 to 01:17:40.6. The value of  $\delta E_M \delta n_e / \langle n_e \rangle$  over this period is significant, compared to the nominal reconnection rate for collisionless reconnection,  $0.1 B_{\text{rec}} V_{\text{Ah}}$  (Birn et al., 2001), indicating a potential importance of the electrostatic LHDW for electron and reconnection dynamics.

## 5 Summary and Discussions

In summary, we present LHDW activity inside a reconnecting current sheet measured by MMS with a moderate guide field. The long-wavelength LHDW exists inside the EDR where  $\beta_e$  is high, while the short-wavelength LHDW exists slightly outside the EDR where  $\beta_e$  is low. The analysis on the wave number  $\mathbf{k}$  shows that  $\mathbf{k}$  has a dominant perpendicular component with a magnitude of  $k \rho_e \sim 0.7$  for  $f \sim f_{\text{LH}}$ , which agrees with features of the fast-growing, short-wavelength LHDW (Davidson et al., 1977). For better understanding of LHDW, we have developed a local theoretical model for the dispersion relation. Overall, results from this model explains the observed LHDW activity, including the magnitude and direction of  $\mathbf{k}$ .

The model is based on the previous work in H. Ji et al. (2005) but improved to include the electron heat flux for better modeling of the perturbed parallel electron pressure, electron temperature anisotropy, parallel electron flow, and independent computation of the perturbed electron density for electrostatic effects. This model can calculate the dispersion with an arbitrary angle between the wave vector and magnetic field, unlike the kinetic treatment of LHDW (Davidson et al., 1977).

The limitation of this local model should be discussed. This analysis assumes no wave propagation along the gradient direction, neglecting the global structure of the current sheet. To address this issue, a global eigenmode analysis (Daughton, 2003; ?) should be carried out, which is our future work. For this event with a large current sheet width, however, this local analysis seems acceptable. The negligible  $k_y$  over  $k_x$  is also supported by the measurement.

This model assumes no temperature gradient for both electrons and ions but the temperature gradient may be important for LHDW activity. With parameters measured

234 in the region B, however, the results are not sensitive against relatively small change in  
 235 the local temperature.

236 This study shows that the short-wavelength LHDW is potentially important for  
 237 electron and reconnection dynamics by generating drag force between electrons and ions  
 238 under a sufficient guide field. Further systematic research on this topic within or near  
 239 the EDR is warranted both in space (i.e. Chen et al., 2019) and in laboratory (i.e. Ste-  
 240 chow et al., 2018).

241 **Acknowledgments**

242 This work was supported by DOE Contract No. DE-AC0209CH11466, NASA grants NNH14AX63I  
 243 and NNH15AB29I, NSF grants AGS-1552142, AGS-1619584, DOE grant DESC0016278,  
 244 NSF-DOE partnership in plasma science grant DE-FG02-00ER54585, and the NASA MMS  
 245 mission. All MMS data used are available at <https://lasp.colorado.edu/mms/sdc/public/>.

246 **References**

247 Birn, J., Drake, J. F., Shay, M. A., Rogers, B. N., Denton, R. E., Hesse, M.,  
 248 ... Pritchett, P. L. (2001). Geospace environmental modeling (gem)  
 249 magnetic reconnection challenge. *J. Geophys. Res.*, 106, 3715. doi:  
 250 doi:10.1029/1999JA900449

251 Carter, T. A., Ji, H., Trintchouk, F., Yamada, M., & Kulsrud, R. M. (2001, Dec.).  
 252 Measurement of lower-hybrid drift turbulence in a reconnecting current sheet.  
 253 *Phys. Rev. Lett.*, 88, 015001. Retrieved from <http://link.aps.org/doi/10.1103/PhysRevLett.88.015001> doi: 10.1103/PhysRevLett.88.015001

254 Cassak, P. A., & Shay, M. A. (2007). Scaling of asymmetric magnetic reconnection:  
 255 General theory and collisional simulations. *Phys. Plasmas*, 14(10), 102114. Re-  
 256 trieval from <http://link.aip.org/link/?PHP/14/102114/1> doi: 10.1063/1  
 257 .2795630

258 Chen, L.-J., Hesse, M., Wang, S., Gershman, D., Ergun, R. E., Burch, J., ...  
 259 Avanov, L. (2017). Electron diffusion region during magnetopause recon-  
 260 nection with an intermediate guide field: Magnetospheric multiscale observa-  
 261 tions. *Journal of Geophysical Research: Space Physics*, 122(5), 5235-5246.  
 262 Retrieved from <https://agupubs.onlinelibrary.wiley.com/doi/abs/10.1002/2017JA024004> doi: 10.1002/2017JA024004

265 Chen, L.-J., Wang, S., Hesse, M., Ergun, R. E., Moore, T., Giles, B., ... Lindqvist,  
266 P.-A. (2019). Electron diffusion regions in magnetotail reconnection un-  
267 der varying guide fields. *Geophysical Research Letters*, 46(12), 6230-6238.  
268 Retrieved from <https://agupubs.onlinelibrary.wiley.com/doi/abs/10.1029/2019GL082393> doi: 10.1029/2019GL082393

270 Daughton, W. (2003). Electromagnetic properties of the lower-hybrid drift instabil-  
271 ity in a thin current sheet. *Phys. Plasmas*, 10(8), 3103–3119. Retrieved from  
272 <http://scitation.aip.org/content/aip/journal/pop/10/8/10.1063/1.1594724> doi: <http://dx.doi.org/10.1063/1.1594724>

274 Davidson, R., Gladd, N., Wu, C., & Huba, J. (1977). Effects of finite plasma beta on  
275 the lower-hybrid drift instability. *Phys. Fluids*, 20, 301.

276 Ergun, R. E., Chen, L.-J., Wilder, F. D., Ahmadi, N., Eriksson, S., Usanova,  
277 M. E., ... Wang, S. (2017). Drift waves, intense parallel electric fields,  
278 and turbulence associated with asymmetric magnetic reconnection at the  
279 magnetopause. *Geophys. Res. Lett.*, 44(7), 2978–2986. Retrieved from  
280 <http://dx.doi.org/10.1002/2016GL072493> doi: 10.1002/2016GL072493

281 Ergun, R. E., Tucker, S., Westfall, J., Goodrich, K. A., Malaspina, D. M., Sum-  
282 mers, D., ... Cully, C. M. (2016, Mar 01). The axial double probe and fields  
283 signal processing for the mms mission. *Space Science Reviews*, 199(1), 167–  
284 188. Retrieved from <https://doi.org/10.1007/s11214-014-0115-x> doi:  
285 10.1007/s11214-014-0115-x

286 Fox, W., Sciortino, F., v. Stechow, A., Jara-Almonte, J., Yoo, J., Ji, H., & Ya-  
287 mada, M. (2017, Mar). Experimental verification of the role of elec-  
288 tron pressure in fast magnetic reconnection with a guide field. *Phys. Rev.*  
289 *Lett.*, 118, 125002. Retrieved from <https://link.aps.org/doi/10.1103/PhysRevLett.118.125002> doi: 10.1103/PhysRevLett.118.125002

291 Graham, D. B., Khotyaintsev, Y. V., Norgren, C., Vaivads, A., André, M., Toledo-  
292 Redondo, S., ... Burch, J. L. (2017). Lower hybrid waves in the ion diffusion  
293 and magnetospheric inflow regions. *J. Geophys. Res.*, 122(1), 517–533. Re-  
294 tried from <http://dx.doi.org/10.1002/2016JA023572> (2016JA023572)  
295 doi: 10.1002/2016JA023572

296 Haaland, S. E., Sonnerup, B. U. Ö., Dunlop, M. W., Balogh, A., Georgescu, E.,  
297 Hasegawa, H., ... Vaivads, A. (2004). Four-spacecraft determination

298 of magnetopause orientation, motion and thickness: comparison with re-  
299 sults from single-spacecraft methods. *Ann. Geophys.*, 22(4), 1347–1365.  
300 Retrieved from <http://www.ann-geophys.net/22/1347/2004/> doi:  
301 10.5194/angeo-22-1347-2004

302 Ji, H., Kulsrud, R., Fox, W., & Yamada, M. (2005). An obliquely propagating elec-  
303 tromagnetic drift instability in the lower hybrid frequency range. *J. Geophys.*  
304 *Res.*, 110, A08212.

305 Ji, H., Terry, S., Yamada, M., Kulsrud, R., Kuritsyn, A., & Ren, Y. (2004, Mar.).  
306 Electromagnetic fluctuations during fast reconnection in a laboratory plasma.  
307 *Phys. Rev. Lett.*, 92, 115001. Retrieved from <http://link.aps.org/doi/10.1103/PhysRevLett.92.115001> doi: 10.1103/PhysRevLett.92.115001

309 Ji, J.-Y., & Joseph, I. (2018). Electron parallel closures for the 3 + 1 fluid model.  
310 *Phys. Plasmas*, 25(3), 032117. Retrieved from <https://doi.org/10.1063/1.5014996> doi: 10.1063/1.5014996

312 Le Contel, O., Leroy, P., Roux, A., Coillot, C., Alison, D., Bouabdellah, A., ... de la  
313 Porte, B. (2016, Mar 01). The search-coil magnetometer for mms. *Space Sci-  
314 ence Reviews*, 199(1), 257–282. Retrieved from <https://doi.org/10.1007/s11214-014-0096-9> doi: 10.1007/s11214-014-0096-9

316 Lindqvist, P.-A., Olsson, G., Torbert, R. B., King, B., Granoff, M., Rau, D.,  
317 ... Tucker, S. (2016, Mar 01). The spin-plane double probe electric  
318 field instrument for mms. *Space Science Reviews*, 199(1), 137–165. Re-  
319 tried from <https://doi.org/10.1007/s11214-014-0116-9> doi:  
320 10.1007/s11214-014-0116-9

321 Mozer, F. S., Angelopoulos, V., Bonnell, J., Glassmeier, K. H., & McFadden, J. P.  
322 (2008). Themis observations of modified hall fields in asymmetric magnetic  
323 field reconnection. *Geophys. Res. Lett.*, 35(17), L17S04. Retrieved from  
324 <http://dx.doi.org/10.1029/2007GL033033> doi: 10.1029/2007GL033033

325 Mozer, F. S., Wilber, M., & Drake, J. F. (2011). Wave associated anomalous  
326 drag during magnetic field reconnection. *Phys. Plasmas*, 18(10), 102902.  
327 Retrieved from <http://link.aip.org/link/?PHP/18/102902/1> doi:  
328 10.1063/1.3647508

329 Norgren, C., Vaivads, A., Khotyaintsev, Y. V., & André, M. (2012, Jul). Lower hy-  
330 brid drift waves: Space observations. *Phys. Rev. Lett.*, 109, 055001. Retrieved

331 from <https://link.aps.org/doi/10.1103/PhysRevLett.109.055001> doi:  
332 10.1103/PhysRevLett.109.055001

333 Pollock, C., Moore, T., Jacques, A., Burch, J., Gliese, U., Saito, Y., ... Zeuch, M.  
334 (2016, Mar 01). Fast plasma investigation for magnetospheric multiscale.  
335 *Space Science Reviews*, 199(1), 331–406. Retrieved from <https://doi.org/10.1007/s11214-016-0245-4> doi: 10.1007/s11214-016-0245-4

336 Pritchett, P. L. (2008). Collisionless magnetic reconnection in an asymmetric cur-  
337 rent sheet. *J. Geophys. Res.*, 113(A6), A06210. Retrieved from <http://dx.doi.org/10.1029/2007JA012930> doi: 10.1029/2007JA012930

338 Pritchett, P. L., & Coroniti, F. V. (2004, January). Three-dimensional collisionless  
339 magnetic reconnection in the presence of a guide field. *J. Geophys. Res.*, 109,  
340 1220.

341 Ricci, P., Blackbill, J., Daughton, W., & Lapenta, G. (2004). Influence of the lower  
342 hybrid drift instability on the onset of magnetic reconnection. *Phys. Plasmas*,  
343 11, 4489.

344 Roytershteyn, V., Daughton, W., Karimabadi, H., & Mozer, F. S. (2012, May).  
345 Influence of the lower-hybrid drift instability on magnetic reconnection in  
346 asymmetric configurations. *Phys. Rev. Lett.*, 108, 185001. Retrieved from  
347 <http://link.aps.org/doi/10.1103/PhysRevLett.108.185001> doi:  
348 10.1103/PhysRevLett.108.185001

349 Roytershteyn, V., Dorfman, S., Daughton, W., Ji, H., Yamada, M., & Karimabadi,  
350 H. (2013). Electromagnetic instability of thin reconnection layers: Comparison  
351 of three-dimensional simulations with mrx observations. *Phys. Plasmas*, 20(6),  
352 -. Retrieved from <http://scitation.aip.org/content/aip/journal/pop/20/6/1.4811371> doi: <http://dx.doi.org/10.1063/1.4811371>

353 Russell, C. T., Anderson, B. J., Baumjohann, W., Bromund, K. R., Dearborn,  
354 D., Fischer, D., ... Richter, I. (2016, Mar 01). The magnetospheric mul-  
355 tiscale magnetometers. *Space Science Reviews*, 199(1), 189–256. Re-  
356 tried from <https://doi.org/10.1007/s11214-014-0057-3> doi:  
357 10.1007/s11214-014-0057-3

358 Santolík, O., Parrot, M., & Lefèuvre, F. (2003). Singular value decomposition meth-  
359 ods for wave propagation analysis. *Radio Science*, 38(1), 1010. Retrieved from  
360 <http://dx.doi.org/10.1029/2000RS002523> doi: 10.1029/2000RS002523

364 Stechow, A. v., Fox, W., Jara-Almonte, J., Yoo, J., Ji, H., & Yamada, M. (2018).  
365 Electromagnetic fluctuations during guide field reconnection in a labo-  
366 ratory plasma. *Physics of Plasmas*, 25(5), 052120. Retrieved from  
367 <https://doi.org/10.1063/1.5025827> doi: 10.1063/1.5025827

368 Tharp, T. D., Yamada, M., Ji, H., Lawrence, E., Dorfman, S., Myers, C. E., &  
369 Yoo, J. (2012, Oct). Quantitative study of guide-field effects on hall recon-  
370 nection in a laboratory plasma. *Phys. Rev. Lett.*, 109, 165002. Retrieved  
371 from <http://link.aps.org/doi/10.1103/PhysRevLett.109.165002> doi:  
372 10.1103/PhysRevLett.109.165002

373 Torrence, C., & Compo, G. P. (1998). A practical guide to wavelet analysis. *Bul-  
374 letin of the American Meteorological Society*, 79(1), 61–78. Retrieved from  
375 [https://doi.org/10.1175/1520-0477\(1998\)079<0061:APGTWA>2.0.CO;2](https://doi.org/10.1175/1520-0477(1998)079<0061:APGTWA>2.0.CO;2)  
376 doi: 10.1175/1520-0477(1998)079<0061:APGTWA>2.0.CO;2

377 Yamada, M., Kulsrud, R., & Ji, H. (2010, Mar). Magnetic reconnection. *Rev. Mod.  
378 Phys.*, 82, 603–664. Retrieved from <http://link.aps.org/doi/10.1103/RevModPhys.82.603>  
379 doi: 10.1103/RevModPhys.82.603

380 Yoo, J., Jara-Almonte, J., Yerger, E., Wang, S., Qian, T., Le, A., ... Gersh-  
381 man, D. J. (2018). Whistler wave generation by anisotropic tail electrons  
382 during asymmetric magnetic reconnection in space and laboratory. *Geo-  
383 physical Research Letters*, 45(16), 8054-8061. Retrieved from <https://agupubs.onlinelibrary.wiley.com/doi/abs/10.1029/2018GL079278> doi:  
384 10.1029/2018GL079278

385 Yoo, J., Wang, S., Yerger, E., Jara-Almonte, J., Ji, H., Yamada, M., ... Alt,  
386 A. (2019). Whistler wave generation by electron temperature anisotropy  
387 during magnetic reconnection at the magnetopause. *Physics of Plasmas*,  
388 26(5), 052902. Retrieved from <https://doi.org/10.1063/1.5094636> doi:  
389 10.1063/1.5094636

390 Yoo, J., & Yamada, M. (2012). Experimental evaluation of common spacecraft data  
391 analysis techniques for reconnection region analysis in a laboratory plasma. *J.  
392 of Geophys. Res.*, 117(A12), A12202. Retrieved from <http://dx.doi.org/10.1029/2012JA017742> doi: 10.1029/2012JA017742

393 Yoo, J., Yamada, M., Ji, H., Jara-Almonte, J., & Myers, C. E. (2014). Bulk ion  
394 acceleration and particle heating during magnetic reconnection in a lab-

manuscript submitted to *Geophysical Research Letters*

397 oratory plasma. *Phys. Plasmas*, 21(5), 055706. Retrieved from <http://scitation.aip.org/content/aip/journal/pop/21/5/10.1063/1.4874331>  
398 doi: <http://dx.doi.org/10.1063/1.4874331>

400 Yoo, J., Yamada, M., Ji, H., Jara-Almonte, J., Myers, C. E., & Chen, L.-J. (2014,  
401 Aug). Laboratory study of magnetic reconnection with a density asymme-  
402 try across the current sheet. *Phys. Rev. Lett.*, 113, 095002. Retrieved  
403 from <http://link.aps.org/doi/10.1103/PhysRevLett.113.095002> doi:  
404 [10.1103/PhysRevLett.113.095002](https://doi.org/10.1103/PhysRevLett.113.095002)